

Hierarchical layered titanate microspherulite: formation by electrochemical spark discharge spallation and application in aqueous pollutant treatment†

Yuxin Tang,^{ab} Dangguo Gong,^a Yuekun Lai,^{ac} Yiqiang Shen,^a Yanyan Zhang,^a Yizhong Huang,^a Jie Tao,^b Changjian Lin,^c Zhili Dong^{*a} and Zhong Chen^{*a}

Received 24th June 2010, Accepted 12th August 2010

DOI: 10.1039/c0jm02005b

An ultrafast and template-free method to synthesize three-dimensional (3D) hierarchical layered titanate microspherulite (TMS) particles with high surface area is reported. The synthesis makes use of an electrochemical spark discharge spallation (ESDS) process, during which a fast anodic reaction on the titanium surface creates a layer of titanium dioxide that instantly breaks down by the applied electrical field into the solution in the form of titanium oxide particles. The spalled particles readily react with the heated NaOH electrolyte to form the titanate particles. A typical as-prepared TMS with a diameter of 0.4–1.5 μm is synthesized by ESDS of Ti foils in 10 M NaOH solution under an applied current density of 0.5 A cm^{-2} , leading to a reaction yield of approximately 0.10–0.15 g per square centimetre of exposed Ti foil within 20 min. After hydrogen ion exchange, the surface area can reach as high as $\sim 406 \text{ m}^2 \text{ g}^{-1}$. On the Ti surface, a crystalline rutile TiO_2 nanosheet structure is formed, which is attributed to the local exothermic heat caused by the spark discharge. A formation mechanism of the TMS is discussed based on field emission scanning electron microscopy (FESEM), a transmission electron microscopy (TEM) study and Raman scattering spectroscopy analysis. The as-prepared TMS shows excellent adsorption performance compared with a titanate micro-particle (TMP), nanowire (TNW) and nanotube (TNT) when methylene blue (MB) and Pb^{II} ions are used as representative organic and inorganic pollutants. The mechanism of adsorption has also been discussed.

Introduction

In recent years, hierarchically structured materials with various morphologies have attracted great attention.¹ Different types of nanostructures, such as column arrays, polyhedron-like particles, belt-branched, core-shell spheres, and vesicles, have been synthesised using functional materials such as SiO_2 , TiO_2 , SnO_2 , MnO_2 , and carbon. The synthesis methods vary from template-assisted growth to solvothermal or other solution-based, template-free processes.^{1,2} The formation of hierarchical structure is generally considered to be a self-assembly process, in which building blocks, *i.e.*, nanoparticles (0D), nanofibers or nanotubes (1D), and nanosheets (2D) self-assemble into regular higher level structures. Many investigations have demonstrated that hierarchical structures could improve the performance of materials in optoelectronic, biomedical, absorption, magnetic applications and energy storage due to their highly porous structure with a large specific surface area.^{2–4} In all these cases,

the controlled synthesis of a 3D nanostructure plays an important role to achieve the advanced materials application targets.

Layered titanate nanomaterials, traditionally synthesised by an alkaline hydrothermal process,⁵ have shown excellent properties for ion-exchange, molecular absorption, photoelectricity and wettability contrast.⁶ So far, the synthesis of 1D and 2D titanate nanomaterials has been widely investigated. For example, 1D titanate nanotubes,^{6e,7} fibers/wires,^{6a} belts,⁸ and rods,⁹ have been synthesized by a hydrothermal method. The drawbacks of this method include the requirement of a high pressure vessel, heating (typically 100–200 °C), and a relatively long processing time (10–120 h),^{6d,10} which poses a limit on the productivity and often results in high production cost. Other researchers have used either a molten-salt synthesis of a TiO_2 mixture at 825 °C for 3 h^{8c} or high-temperature oxidation of NaOH coated Ti foils at 800 °C for 1.5 h in the presence of O_2 and H_2O vapor.⁹ The 2D titanate nanosheets have also been prepared by a one step hydrothermal route¹¹ or a two-step approach involving the titanate formation and exfoliation.¹² So far it remains a great challenge to produce 3D hierarchically elaborate shapes of titanate over multiple scales and the synthesis is usually not straightforward.^{3,11,13} Recently, Cao *et al.*¹¹ synthesized titanate flowers *via* a template-assisted approach through a hydrothermal reaction between a NaOH solution and a mixture of TiO_2 and $\text{Zn}(\text{NO}_3)_2 \cdot 6\text{H}_2\text{O}$. Titanate flowers formed after removing the ZnO flower-like nanorod framework. Yoshikawa *et al.*¹⁴ reported a two-step method combining hydrolysis of titanium tetraisopropoxide with the hydrothermal treatment of amorphous TiO_2 spheres to prepare flower-like titanate nanosheets. Imai's group³ had explored various kinds of

^aSchool of Materials Science and Engineering, Nanyang Technological University, 50 Nanyang Avenue, Singapore, 639798, Singapore. E-mail: aszchen@ntu.edu.sg; zldong@ntu.edu.sg; Fax: +65 6790 9081; Tel: +65 6790 6727; +65 6790 4256

^bCollege of Material Science and Technology, Nanjing University of Aeronautics and Astronautics, 29 Yudao Street, Nanjing, 210016, China

^cState Key Laboratory of Physical Chemistry of Solid Surfaces and College of Chemistry and Chemical Engineering, Xiamen University, Xiamen, 361005, China

† Electronic Supplementary Information (ESI) available: Additional data for materials characterization and degradation performance. See DOI: 10.1039/c0jm02005b/

hierarchical ammonium titanate nanosheet morphologies grown in an agar gel medium by a bottom-up route. Mao and co-workers¹³ demonstrated the growth of micrometre scale seaurchin-like structures by an oxidizing H₂O₂-assisted hydrothermal method in an autoclave at different temperatures and durations. They proposed a two-stage growth mechanism for the formation of titanate spheres. Self-assembled titanate nanosheets were also synthesized *via* a chimie-douce method by refluxing TiO₂ powder in 15 M NaOH at 423 K for more than 24 h.¹⁵ Moreover, Xie's group used the Kirkendall effect to construct 3D hollow titanate tubular hierarchical structures by treating a TiCl₄ precursor in other alkaline solutions (*e.g.*, ethylenediamine) at 225 °C for 12 h.¹⁶ Despite the 3D complex structures that have been achieved by these methods, a facile and inexpensive scheme for the controlled morphologies with well defined hierarchical 3D structures is still lacking and will be of great interest to researchers in the field.

So far, the hydrothermal route appears to be most popular for the synthesis of 1D, 2D and 3D titanate materials. The efficacy of the hydrothermal vessel notwithstanding, conventional glassware is more readily accessible to many nanotechnology scientists and chemists and less costly. Some existing approaches require multiple steps or a long processing time to ensure complete reaction,^{3–16} *e.g.*, the time taken for the reaction between agar gel with Ti precursor and NH₄OH is one week.³ Other methods like molten-salt synthesis^{8c} and high-temperature oxidation⁹ involve complicated processes and/or high temperature (>800 °C). All these have posed a limitation to the practical application of these materials that have shown excellent performance. It is well known that a porous TiO₂ layer can be formed on a Ti foil surface by electrochemical anodization¹⁷ or plasma electrolytic oxidation¹⁸ of Ti foils. Inspired by these works, we develop a novel one-pot approach to produce highly porous hierarchical 3D titanate micro-spherulite (TMS) particles *via* a simple, high throughput method simultaneously employing electrochemical anodization and spark discharge of the anodized oxide layer into a reactive solution by carefully adjusting the applied electrical spark parameters in a traditional ambience setup,¹⁹ which is shown in Fig. 1. Additionally, when used as an

adsorbent in waste-water treatment, the as-prepared layered titanate TMS exhibits a good ability to remove methylene blue dye and toxic lead ions.

Experimental

Preparation of materials

TMS particles were prepared from a starting titanium foil (0.25 mm thickness, 99.7% purity purchased from Aldrich Corporation) *via* a rapid ESDS method^{19a} in an electrolyte of 10 M sodium hydroxide (NaOH) in aqueous solution using a platinum counter-electrode (99% purity Alfa-Aesar Corporation, Ward Hill, MA), as shown in Fig. 1. The anodization was conducted in the galvanostatic mode at current density ranges from 0.25 to 1.0 A cm⁻² at room temperature (about 25 °C), and the distance between two electrodes was 3 cm. To ensure lab safety, the experiments should be carried out in a fume hood with good ventilation so that any generated gases (*e.g.*, H₂) can be instantly removed. The exposed area of Ti foil was about 2 cm² for all the experiments. Prior to the experiment, the titanium foil was degreased by alcohol and cleaned by deionized (DI) water. Then it was chemically polished by the polishing solution composed of concentrated nitric acid and hydrofluoric acid mixed at 1 : 1 proportion by volume. The titanium foil was cleaned again by DI water and dried by N₂ gas before the experiment. In order to investigate the electrochemical spallation behaviour and the variation of solution temperature, the temporal evolutions of anodic voltage and the solution temperature with time were obtained by using a digital multimeter and thermometer recorder interfaced with a computer respectively. After completion of the experiment, a grey white precipitate, collected from the solution, was centrifuged and washed with DI water until the pH value of the solution was around 7. The hydrogen titanate was obtained by soaking the precipitates in HCl solution (0.1 M) for 3 h, followed by washing in DI water and absolute ethanol and drying in air. The process was repeated 3 times. The surface of Ti foil was repeatedly rinsed with DI water and subsequently dried by N₂ gas prior to FESEM observation.

Sample characterization

The morphologies of the as-synthesized TMS particles and Ti surface after anodization were investigated by a field emission scanning electronic microscope (FESEM, JEOL JSM-6340F). A transmission electron microscope (TEM, JEOL JEM-2010) operating at 200 kV was used to characterize the detailed nanostructures. Energy dispersive X-ray analysis was carried out in attachments in the TEM and FESEM. A Shimadzu 6000 X-ray diffractometer with a Cu K α source was used for phase identification. Nitrogen adsorption/desorption isotherms were measured at 77 K using ASAP2000 adsorption apparatus from Micromeritics. The samples were degassed at 373 K for 4 h under vacuum before analysis. Raman measurements were performed at room temperature in a WITEC confocal spectrometer with a 488 nm excitation laser operated at a low power level (1 mW), and the Si peak at 520 cm⁻¹ was used as a reference for the wave number calibration.

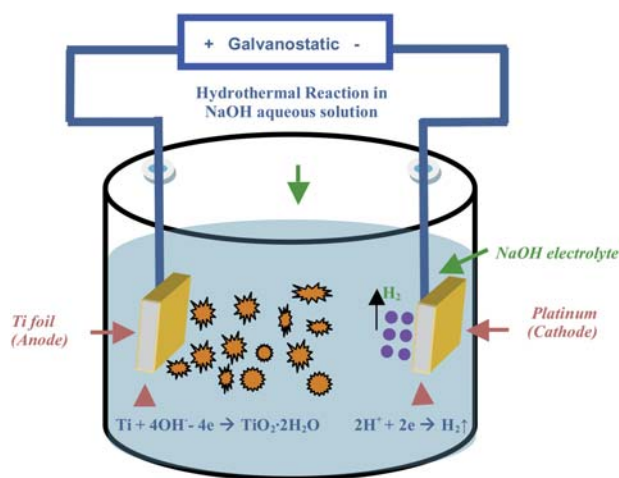


Fig. 1 Schematic representation of a reaction process by electrochemical spark discharge spallation of a starting Ti foil.

Adsorption test

In order to determine and compare the adsorption performance of the as-synthesized TMS, TMP, TNW and TNT samples, the heavy toxic Pb^{II} and methylene blue (MB) were selected. All the adsorption experiments were conducted at stirring condition throughout the test at room temperature ($25\text{ }^{\circ}\text{C}$) in the dark. For the MB dye, the equilibrium adsorption isotherm was determined by a concentration variation method. The experiment was carried out with 50 mL of MB solution with varying concentration from 20 to 100 ppm. In each run, 10 mg of adsorbent was added to the solutions. The pH value was within the range 9.5~10. After 72 h, equilibrium was reached and the equilibrium concentration was measured. The sorption kinetics test was done with 100 mL of MB solution with an initial concentration of 20 ppm. In each run, 10 mg of the synthesized powder was added. The quantitative determination of the MB concentration in solution at different time intervals was performed by measuring the intensity change absorption peak (at 665 nm) of the sample solution under a Perkin-Elmer UV-Vis-NIR Lambda 900 spectrophotometer.

The Pb^{II} exchange isotherm was measured by equilibrating 20 mg of the adsorbents in 50 mL of $\text{Pb}(\text{NO}_3)_2$ having concentration range of $0.1\sim 2.0 \times 10^{-3}\text{ M}$ for 72 h. The initial pH value of the prepared solutions was adjusted at about 5.0~5.5 during the sorption process to avoid the formation of PbCO_3 or $\text{Pb}(\text{OH})_2$ on the titanate surface. The sorption kinetics was also investigated. 5 mL Pb^{II} suspension solution after equilibrating an adsorbent with the solution were collected at 5, 10, 20, 30, 60 and 120 min, respectively. The collected samples were centrifuged and filtered, and the concentrations of Pb^{II} were determined by inductively coupled plasma atomic emission spectroscopy (ICP-OES).

Result and discussions

Electrochemical spark discharge spallation behavior

The temporal evolutions of anodic voltage and the solution temperature with time at different current densities are shown in Fig. 2. In the current setup, the applied anodization voltage (27.0~31.5 V, Fig. 2a) is higher than the experimental breakdown voltage of TiO_2 ($\sim 25\text{ V}$) in a 10 M NaOH solution. Therefore, the oxide layer at the electrolyte/oxide interface is electrically broken down and spalled into the solution in the form of small precipitates by the generated spark discharge. The electrochemical spallation behaviour can be explained in the light of the voltage- and temperature-time plots, as follows. At the early stage in Fig. 2a, the dielectric breakdown occurs and the voltage increases linearly with anodization time. The linear increase of the voltage and the galvanostatic oxide thickness can be explained by the well-known high field-assisted ionic transport mechanism.²³ The relationship between the anodic current and the electric field strength across the anodic oxide film is described by

$$I = A \cdot \exp(B \cdot U/d) \quad (1)$$

where I is the ionic current, A and B are electrolytic constants, U is the forming voltage and d is the anodic oxide thickness. During

galvanostatic anodization, a constant electric field strength (U/d) across the previously formed barrier film is required in order to maintain the given constant current density. When the anodization starts, a TiO_2 oxide layer is formed due to interaction of the surface Ti^{4+} ions with hydroxyl ions (OH^-) in the solution.¹⁷⁻¹⁹ As a consequence, when the oxide thickness increases with time at a constant current density, the voltage across the oxide film increases in order to maintain the current density. This explains the linear increase of the voltage at the beginning as shown in Fig. 2a. Initially, it is found that the higher anode voltage is needed when the anodization is conducted at higher current density, and this trend is changed with the increase of solution temperature. The gradual increase of the solution temperature caused by the exothermic reaction is observed in Fig. 2b. Based on Ohm's law, the total resistance for the anodization system $R = R_c + R_{a/e} + R_e + R_{c/e}$, where R_c is the resistance of the circuit, $R_{a/e}$ is the resistance of anode/electrolyte interface, R_e the resistance of electrolyte, and $R_{c/e}$ the resistance of cathode/electrolyte interface. $R_{a/e} + R_e$ changes all the time and will influence the total R during the process. During the spark discharge process, R_e decreases as the temperature rise accelerates the ionic mobility of the electrolyte, and $R_{a/e}$ is also decreased due to the spallation

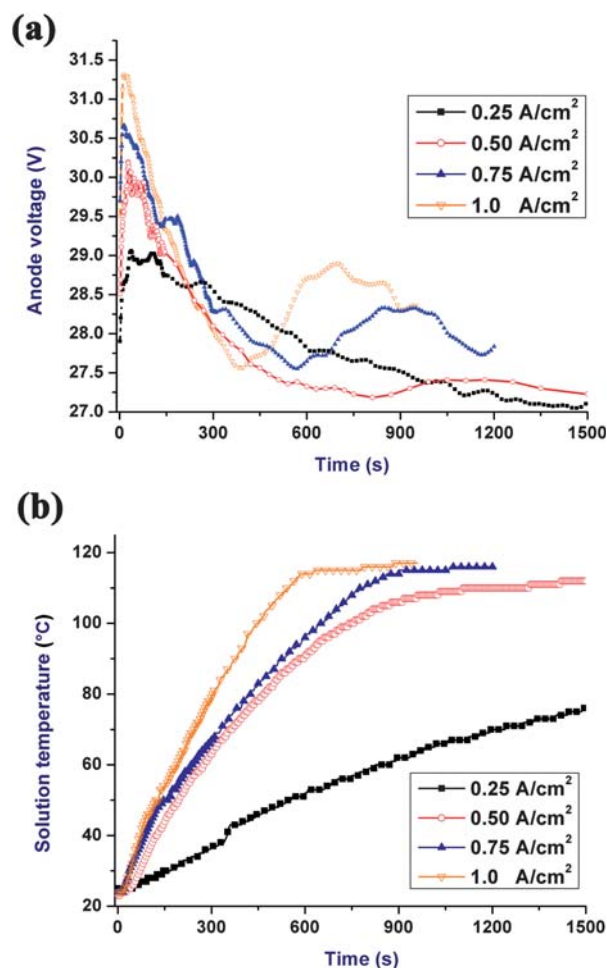


Fig. 2 Dependence of the anodic voltage (curve a) and solution temperature (curve b) with anodization time in a 10 M NaOH solution under different current densities.

and dissolution of compact TiO_2 layer. Consequently, the anodic voltage ($=I \cdot R$) decreases after reaching the maximum voltage under the constant current density mode. It is also observed that the obvious fluctuation of anode voltage occurs, which is caused by the instantaneous change the total resistance (R) and the drastic evolution of gas from the electrodes during the dielectric breakdown.

The electrochemical spark discharge spallation under different current densities generates different amount of heat derived from the exothermic reaction. When the process is conducted at high current density, the solution temperature increases much faster. For example, under lower current density (0.25 A cm^{-2}), the solution temperature was around 78°C after 25 min anodization due to the limited heat derived from the anode. When the current density rose to 0.5 A cm^{-2} or above, a rapid increase in solution temperature ($\sim 110^\circ\text{C}$) was observed. The XRD result (Fig. S1, ESI †) indicates that the titanate material can be formed at low temperatures ($\sim 78^\circ\text{C}$) under a current density of 0.25 A cm^{-2} . The morphologies of the titanate particles formed under different current densities are quite similar, thus we focus on one of them (0.5 A cm^{-2}) in all subsequent studies.

Characterization of the hierarchical titanate TMS materials

Typical FESEM images of the TMS particles and the porous TiO_2 oxide layer on the Ti foil surface after 20 min electrochemical spark discharge spallation (ESDS) processing at a current density of 0.5 A cm^{-2} are shown in Fig. 3a and Fig. 3b respectively. The electrolyte turned from clear in the beginning of the process to turbid due to the formation of white precipitates.

After the ESDS treatment, the as-prepared sodium-hydrogen TMS (NaH-TMS) particles with diameters ranging from $0.4 \mu\text{m}$ to $1.5 \mu\text{m}$ were well dispersed (Fig. 3a). Many fine structures radiated from the core of the spherulite, and are shown to possess a nano-flake structure. The NaH-TMS could be transformed to hydrogen titanate TMS (H-TMS) with the same morphology after acid washing. Energy dispersive X-ray spectroscopy (EDS) data (Fig. S2, ESI †) provide the supporting evidence for the transformation from NaH-TMS to H-TMS as there was no Na

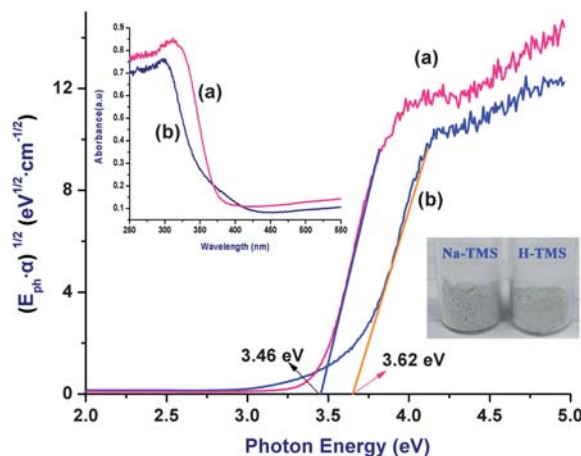


Fig. 4 Tauc's plots for band gap determination of as-prepared (a) H-TMS and (b) NaH-TMS samples anodized at a current density of 0.5 A cm^{-2} ; the insets show their UV-visible diffuse reflectance spectra (left) and the digital photos (right).

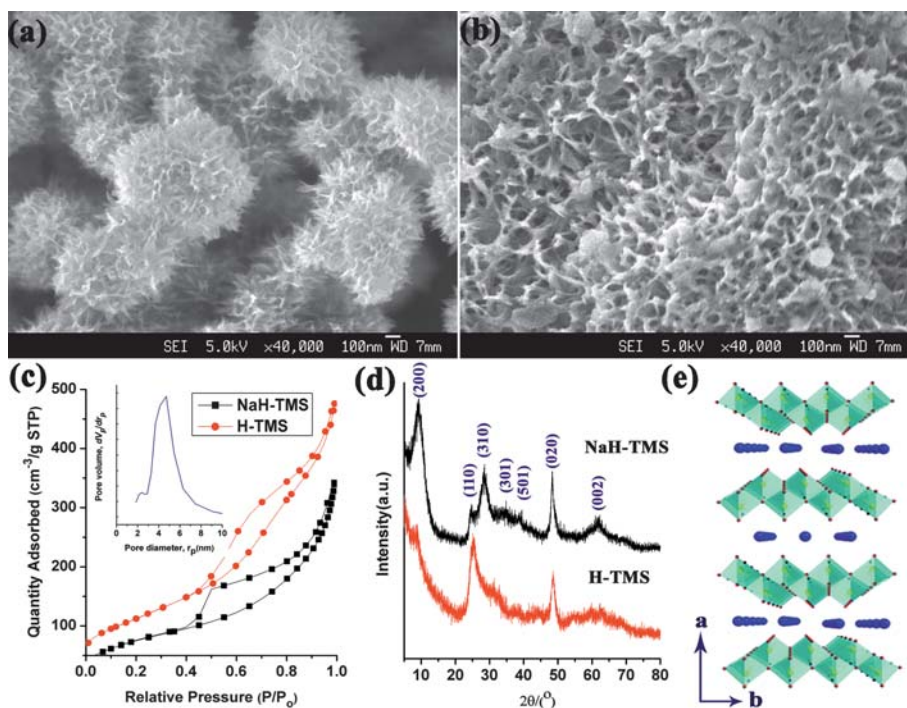


Fig. 3 FESEM images of the synthesized (a) NaH-TMS; (b) porous TiO_2 layer left on Ti foil surface by ESDS method in 10 M NaOH solution for 20 min; (c) isotherm nitrogen sorption of NaH-TMS and H-TMS; (d) XRD patterns of as-prepared NaH-TMS and H-TMS; (e) polyhedral representation of orthorhombic $\text{Na}_x\text{H}_{2-x}\text{Ti}_2\text{O}_5 \cdot \text{H}_2\text{O}$. Interlayer water molecules (H_2O) are not shown. The dot between the layers is Na^+ or H^+ . The samples were anodized at a current density of 0.5 A cm^{-2} . The inset in (c) shows a pore volume distribution of H-TMS (BJH desorption).

element in the H-TMS sample. The optical band gaps of NaH-TMS and H-TMS are evaluated from Tauc's plot, shown in Fig. 4. Their UV-Vis adsorption spectra and digital photos are shown in the insets of Fig. 4. Semiconductors absorb light below a threshold wavelength, the fundamental absorption edge, which is related to the band gap energy (E_g) via

$$E_g \text{ (eV)} = 1240 / \lambda_g \text{ (nm)} \quad (2)$$

For a direct band gap transition of titanate materials, the absorption coefficient (α) is related to the photon energy (E_{ph}) via

$$(E_{ph} \cdot \alpha) = B (E_{ph} - E_g)^{0.5} \quad (3)$$

From the Tauc plot of $(E_{ph} \cdot \alpha)^{0.5}$ vs. E_{ph} , the band gap energy can be determined by extrapolating the linear region. Calculated from the above equations, the onset wavelengths of NaH-TMS and H-TMS are about 342 nm and 358 nm, corresponding to the band gap value of 3.62 eV and 3.46 eV respectively. These values are in the same range with previous reports of titanates.²⁰ Typical isotherms for nitrogen adsorption and desorption on the surfaces of the as-prepared NaH-TMS and H-TMS conducted at 77 K are shown in Fig. 3c, and the Barrett–Joyner–Halenda (BJH) pore size distribution is shown in the inset. Interestingly, typical type-IV N_2 sorption isotherms with a distinctly increasing step in the middle relative pressures were observed for NaH-TMS and H-TMS, characteristic of mesoporous structure (Fig. 3c).⁴ The NaH-TMS has a high Brunauer–Emmett–Teller (BET) surface area of 277.52 $m^2 g^{-1}$ with a pore volume of 0.52 $cm^3 g^{-1}$. The average pore size of the NaH-TMS is about 7.5 nm. After acid washing, the H-TMS materials show higher BET surface areas

(406.41 $m^2 g^{-1}$) and larger pore volumes (0.76 $cm^3 g^{-1}$), which come from mesopores of H-TMS possessing a narrow pore size distribution with a peak value of 4.4 nm. The gaps between the thin nano-flakes clearly contribute to the mesoporosity. Fig. 3d shows the crystal structure of the as-prepared TMS. The low diffraction angle at $\approx 9^\circ$ of the NaH-TMS or H-TMS indicates the product possesses a large inter-plane distance, which is common for layered titanate structures. The broad peaks at $2\theta = 9.2^\circ$ ($d = 9.61 \text{ \AA}$), 24.6° ($d = 3.62 \text{ \AA}$), 28.5° ($d = 3.13 \text{ \AA}$), 34.9° ($d = 2.57 \text{ \AA}$), 38.8° ($d = 2.31 \text{ \AA}$), 48.3° ($d = 1.88 \text{ \AA}$), and 62° ($d = 1.50 \text{ \AA}$) of NaH-TMS correspond well with the (200), (110), (310), (301), (501), (020), and (002) planes of orthorhombic $H_2Ti_2O_5 \cdot H_2O$ (JCPDS No. 47-0124). This type of crystal structure consists of lepidocrocite-type host layers (shown in Fig. 3e) similar to those in the layered $H_{0.7}Ti_{1.825}\Delta_{0.175}O_4 \cdot H_2O$ (Δ : vacancy) but with different protons.^{7c,21,22} Moreover, thermogravimetric analysis of the TMS sample shown in Fig. S3 (ESI[†]) implies a strong absorption of water by the titanate: the weight loss of step 1 is due to the evaporation of adsorbed water molecules on the particle surface. The weight loss in step 2 can be attributed to the dehydroxylation of the TMS and the formation of the crystalline TiO_2 .²¹ Based on our measurements, it is reasonable to assign the NaH-TMS and H-TMS as layered $Na_xH_{2-x}Ti_2O_5 \cdot H_2O$ (Fig. 3e) and $H_2Ti_2O_5 \cdot H_2O$ respectively.

Transmission electron microscopy (TEM) images shown in Fig. 5 reveal the morphology of the NaH-TMS (Fig. 5a–c) and H-TMS (Fig. 5d–f). The 3D TMS micro-particle consists of individual 2D titanate flakes at the nanoscale, centred from the core like a star (Fig. 5b) forming a hierarchical morphology. The insets of Fig. 5b and Fig. 5e are the electron diffraction patterns of NaH-TMS and H-TMS spheres respectively. Diffraction rings were observed since the samples were polycrystalline with the

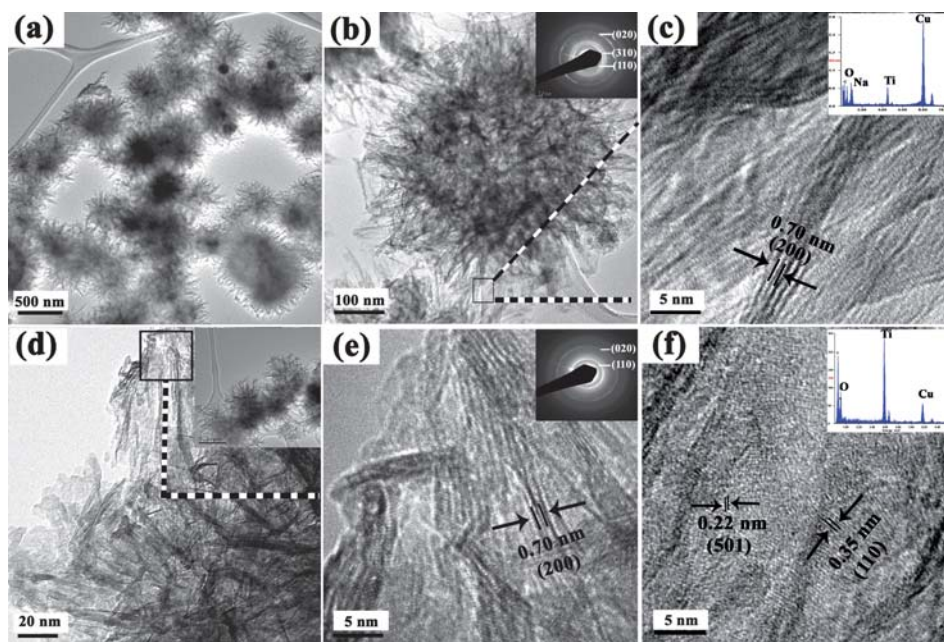


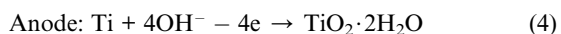
Fig. 5 TEM images of the fabricated (a) NaH-TMS; (b) individual NaH-TMS anodized under a current density of 0.5 $A cm^{-2}$. The inset shows the corresponding electron diffraction pattern; (c) HRTEM of selected square area in (b). The inset provides the EDS spectra; (d) TEM image of H-TMS nano-flakes. The inset shows the morphology of the H-TMS particles; (e) enlarged view of the selected area in (d). The inset shows the corresponding electron diffraction pattern; (f) the plane view of the H-TMS flakes. The inset displays the EDS spectra.

nano-flakes radiating outwards. The three diffraction rings are indexed as coming from the three intensive (110), (310), and (020) diffraction planes for the orthorhombic NaH-TMS, while only two sharp diffraction rings corresponding to the (110) and (020) planes of H-TMS were observed. These results are constant with the XRD results (Fig. 3d). EDS analysis, shown in insets of Fig. 5c and Fig. 5f, suggests that the NaH- and H-TMS are composed of Na/Ti/O and Ti/O individually while the Cu element comes from the copper grid. The FESEM-EDS result in Fig. S2 (ESI†) further verifies the elemental information. Based on the fringes in the high-resolution TEM image of the NaH-TMS in Fig. 5c, the interlayer distance of the layered structure is *ca.* 0.74 nm. It is interesting to note that the morphology of H-TMS, shown in Fig. 5d, is similar to those of Fig. 5a after acid washing. The displayed interlayer distance for H-TMS is lower and close to 0.70 nm (Fig. 5d), which is consistent with the literature reports.^{11,13,15,21} Moreover, the other two fringes with interlayer distances of 0.22 and 0.35 nm in the nano-flakes were observed in Fig. 5f. These three values correspond to the spacing of the (200), (501), and (110) planes of a lepidocrocite $\text{Na}_x\text{H}_{2-x}\text{Ti}_2\text{O}_5 \cdot \text{H}_2\text{O}$ respectively. It is noted that the interlayer distance measured from the TEM image is smaller than that obtained from the XRD measurement. This deviation is caused by the dehydration of the samples in ultrahigh vacuum during the TEM observation.^{6d,11,21} The plane view of nano-flakes, shown in Fig. 5f and Fig. S4 (ESI†), reveals that the individual flakes consist of tapered ends on the flat plane. Furthermore, the nano-flake is mostly crystalline with the presence of tiny amorphous structures at the ends (Fig. S4b, ESI†).

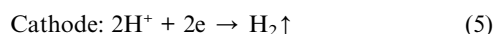
Formation mechanism

To understand the formation process of the TMS, FESEM observation was carried out on both the powders and the Ti foil surface after different anodization times. The morphological evolution process with time is shown in Fig. S5 and Fig. S6 (ESI†) respectively. The dependence of anodic voltage and the solution temperature with time at a current density of 0.5 A cm^{-2} was shown in Fig. 2. Additionally, a series of the powder morphology evolution is shown by TEM in Fig. 6. The Raman scattering spectra (Fig. 7) are also provided to understand the crystal structure evolution with processing time.

When the spark discharge starts, the oxide layer is formed at the electrolyte/oxide interface *via*



Then the layer is electrically broken down and spalled into the solution at relatively high-voltage electrolyzing oxidation process. Simultaneously, a rapid evolution of hydrogen in the form of strong bubbling occurs at the cathode *via*:



This ESDS process induces the formation of crystalline TiO_2 structure, which is triggered by the local exothermic heat caused by the vigorous spark discharge. This is supported by the results of the Raman spectra shown in Fig. 7. The bands located at 144, 198, 398, 515, 640 cm^{-1} of the precipitation collected from the

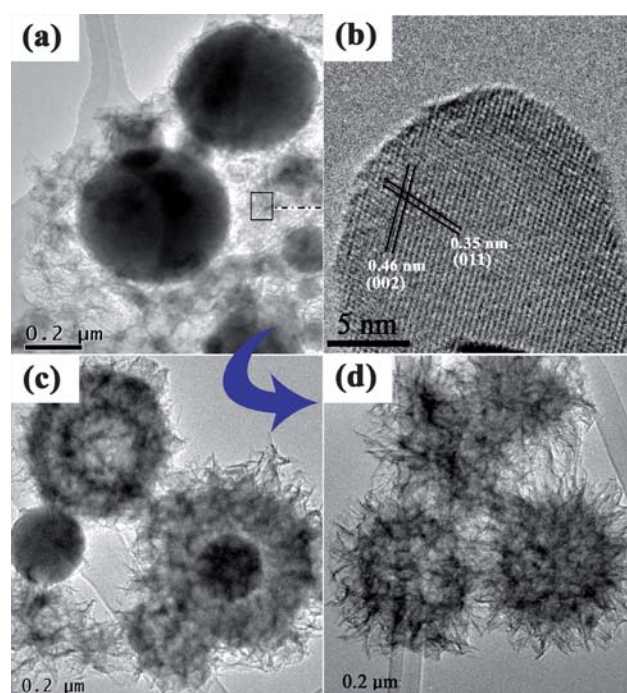


Fig. 6 TEM images of (a,b), (c), (d) powders samples taken at 2, 10 and 20 min under a current density of 0.5 A cm^{-2} respectively. (b) HRTEM image of the selected area in (a).

solution belong to Raman ($\text{A}_{1g} + 2\text{B}_{1g} + 3\text{E}_g$) active modes of the anatase (Fig. 7a, 2 min), and the two fringes with distances of 0.35 nm and 0.46 nm correspond to the spacing of the (011) and (002) planes of anatase TiO_2 are also observed in Fig. 6b. It was observed that the precipitates possess a microscale spherical core. But on the outer layer of the precipitates, there exists many radiating fine structures with high porosity (Fig. 6a, Fig. S5a–d, ESI†). With time, the crystal structure of the precipitates changes from anatase (Fig. 7a, 2 min) to mixed anatase/titanate (Fig. 7a, 2.5 min) and mixed rutile/titanate (Fig. 7a, 3 min) before complete conversion to titanate. This implies that the spalled particles were initially anatase phase, and then became rutile after ~ 3 min. On the other hand, the surface layer left on the Ti foil consists of anatase and rutile in the initial stage (Fig. 7b, 2~5 min) and changes to rutile only later.

When the electrolyte temperature increases, the hydrothermal reaction of the spalled TiO_2 particles begins. Strictly speaking, the conditions are not exactly the same as the ones of a hydrothermal reaction (*e.g.* no high pressure is present in the ESDS process). “Hydrothermal-like” might be more precise to describe the reaction. The reaction also changes the morphology and crystal structure of the spalled particles. The reaction takes place in solution based on the following reaction:



In Fig. 7a, the broad Raman bands located near 188, 280, 389, 447, 705, and 905 cm^{-1} belong to the titanate structure formed after anodization for 4~5 min. These bands remain the same with prolonged treatment duration up to 20 min. The starting titanate formation temperature in the solution was found to be around $60 \text{ }^\circ\text{C}$, which agrees with Kim’s previous report.²⁴ The

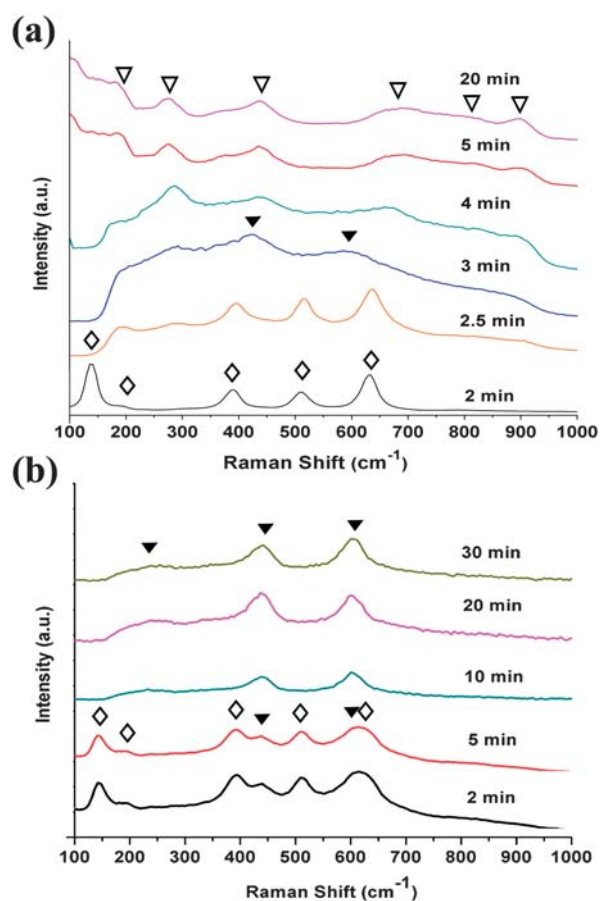


Fig. 7 Raman spectra of (a) the precipitates collected from the solution after 2, 2.5, 3, 4, 5, 20 min anodization; (b) the TiO₂ layer generated on Ti foil after 2, 5, 10, 20, 30 min anodization (◊ — anatase; ▼ — rutile; ▽ — titanate).

titanate-titanate transformation has resulted in the spherulite type of titanate particles consisting of radiating nano-flakes. For example, the titania micro-spherulite (Fig. 6a) formed at 2 min has transformed to a porous spherulite structure with nano-flakes at 10 min (Fig. 6c) due to the hydrothermal-like reaction. As the reaction proceeds (20 min), the retrieved particles almost completely consist of nano-flakes (Fig. 6d). It was also observed that the average size of precipitates decreases as the reaction proceeds, as shown by the FESEM images of powders collected at different times (Fig. S5, ESI†). This is likely due to the decrease of the breakdown thickness of the TiO₂ layer in the heated solution where the voltage applied to the dielectric layer ($=I \cdot R_{a/e}$) decreases. The applied voltage curve conducted at 0.5 A cm⁻² decreases to a steady state in Fig. 2a largely because of the decrease of the dielectric layer voltage.

A layer of crystalline TiO₂ was formed on the Ti foil surface. Its morphology evolved as shown in Fig. S6, ESI†. As a result of the spark discharge, the dense oxide layer starts to spall and dissolve, and the Ti surface becomes rougher with time. More detailed examination shows that numerous cracks or pores were formed on the Ti surface (Fig. S6c–e, ESI†). As the reaction progresses, the increase in temperature resulted in accelerated anodic dissolving TiO₂ films and the formation of nanosheet structures on the Ti surface (Fig. S6i–n, ESI†). Since the TiO₂

layer is continually broken into the solution due to the spark discharge, the surface layer always consists of the freshly formed TiO₂. Thus there is not enough time for the chemical reaction between the TiO₂ and the NaOH solution to occur on the surface of the Ti foil. As a result, no titanate phase was found on the Ti surface (Fig. 7b). The increase of the discharge temperature on the Ti foil surface has promoted the phase transformation of the anodized TiO₂ layer from anatase to rutile. The Raman spectra in Fig. 7b shows surface layer consists of the anatase and rutile TiO₂ at the beginning (2~5 min), and then this crystal structure changes completely to rutile TiO₂ later (10~30 min). The crystalline phase of the spalled particles followed the same sequence (Fig. 7a). Despite the difference in the starting phase of TiO₂, the same titanate phase forms after reaction with high concentration NaOH (Fig. 7a). Our results agree with previous reports that all polymorphs of TiO₂ (anatase, rutile, brookite, or amorphous) can be transformed to the titanate under alkaline hydrothermal conditions.^{6d,10}

On the basis of the experimental results, we propose the following as the formation mechanism of the hierarchical titanate microspherulite in the solution and TiO₂ nanosheet structure on the Ti foil surface. The whole process is through a synergistic effect of electrochemical spallation and hydrothermal-like reaction, as illustrated in Fig. 8. In the first stage (I), fast anodic reaction on titanium surface creates a layer of titania that instantly breaks down under the applied electrical field into the solution in the form of anatase titania particles [Fig. 7a (2 min), Fig. S5a,b]. From the TEM image (Fig. 6a) and SEM image (Fig. S5a,b, ESI†), it is observed that the titania particles possess porous surface features. This would facilitate rapid reaction with the NaOH solution. At the same time, numerous small micro-pores (Fig. S6c–e, ESI†) are formed on Ti foil surface. In the second stage (II), at a relatively high solution temperature (60 °C, 5 min), the porous spalled particles readily react with the heated NaOH electrolyte to form the titanate particles (Fig. 7a, 5~20 min) in stage (II)-(a), and the hierarchical porous structure (Fig. 6c) is gradually derived from the titania precipitate (Fig. 6a). The formation of TMS is ultra fast because the spalled particles can be heated up to extremely high temperature by the spark discharge. It has been reported that the

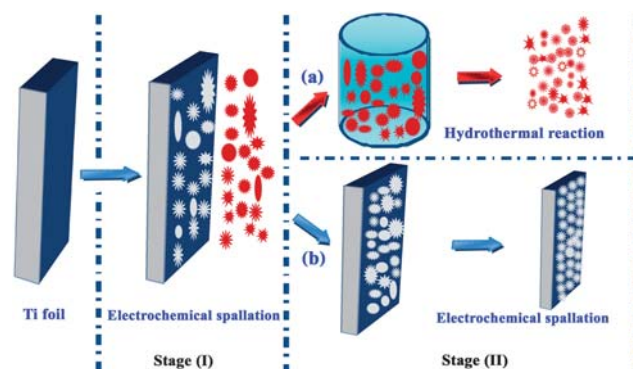


Fig. 8 Schematic illustration of the formation process for TMS and TiO₂ nanosheet structure. Stage I: the formation of TiO₂ particle and TiO₂ oxide layer by anodization and spallation of Ti foils; stage II: (a) the formation of TMS in the solution by hydrothermal-like process; (b) the formation of TiO₂ porous nanosheet on Ti foil surface.

spark discharge can cause local temperature to reach several thousand Kelvin (K).¹⁸ Such a condition is unmatched by any existing methods for titanate formation, which typically take much longer time (12–48 h) for the reaction to complete.^{6,15} Using the reflux method, a similar morphology of flower-like titanate particles has been reported.¹⁵ However, the surface area ($\sim 224 \text{ m}^2 \text{ g}^{-1}$) was lower than our TMS and the reaction took days to complete.¹⁵ In stage (II)-(b), the micropores in the oxide layer on the Ti surface turns into nanosheet structure (Fig. S6i–n, ESI†) as a result of dissolution in the high concentration alkaline solution. This is the first report that crystalline TiO_2 nanosheet is formed at a low applied voltage (around 30 V) compared to the reported high voltage micro-arc oxidation (100–500 V).^{18b,c}

The reported synthesis method is different from all known approaches to form titanate nanostructures. A unique advantage of the current method lies in its high throughput at a simple ambient setup, while most of the reported methods require much longer processing time. The reaction yield of the current method was 0.10–0.15 g TMS per cm^2 of Ti foil for only 20 min processing at a current density of 0.5 A cm^{-2} . The production yield can be easily scaled up by increasing the exposed Ti surface area and the current density. The specific surface area of H-TMS clearly exceeds any reported values of hydrogen titanate materials (e.g., nano-tubes, wires, etc.) prepared by hydrothermal method so far.

Evaluation of the adsorption properties

Materials with layered crystal structures, such as titanates and niobates, could be used as adsorbents or catalysts for the removal of organic and inorganic pollutants in waste water. Very recently, the 1D-titanate nanofibers^{6a} and nanotubes^{6c,25} showed excellent adsorption of organic molecules and radioactive toxic metal ions.^{6d} Divalent lead (Pb^{II}), one of the metals that have the most damaging effects on human health, can cause damage to the central nervous system and dysfunction to the kidneys and immune system of human beings, especially for children.²⁶ As an example of a potential application, the as-obtained micro-scale 3D-TMS was evaluated for adsorption of toxic heavy metal ions Pb^{II} and methylene blue (MB), a common organic dye in the textile industry. For comparison, we also prepared trititanate micro-particle (TMP) *via* pyrosynthesis, titanate nanowire (TNW) and titanate nanotube (TNT) by a hydrothermal approach. All these samples for the adsorption experiments are without acid washing. The experimental condition and morphology of the prepared TMP, TNW and TNT are shown in Fig. S7, ESI† Fig. 9 and Fig. 10 illustrate the absorption performances of different adsorbents for MB and Pb^{II} in aqueous solutions. The as-prepared 3D TMS stands as the best with high removal capacity and adsorption rate of MB compared to TNW, TNT and TMP. TMS can remove 75% MB from the solution in 5 min (Fig. 9a, Fig. S8, ESI†). After 12 h, it completely removed the MB (Fig. 9b). We estimate that 1.0 g as-prepared TMS can remove about 236.2 mg MB (Table 1, Fig. S9, ESI†) based on experimental saturate sorption capacity. The sorption capacity of TMS is slightly larger than the corresponding capacity for titanate TNT (232.2 mg g^{-1} , Table 1) and much higher than the ones by the TMP and TNW. The removal capacity was significantly higher than what was reported for a 3D hierarchical

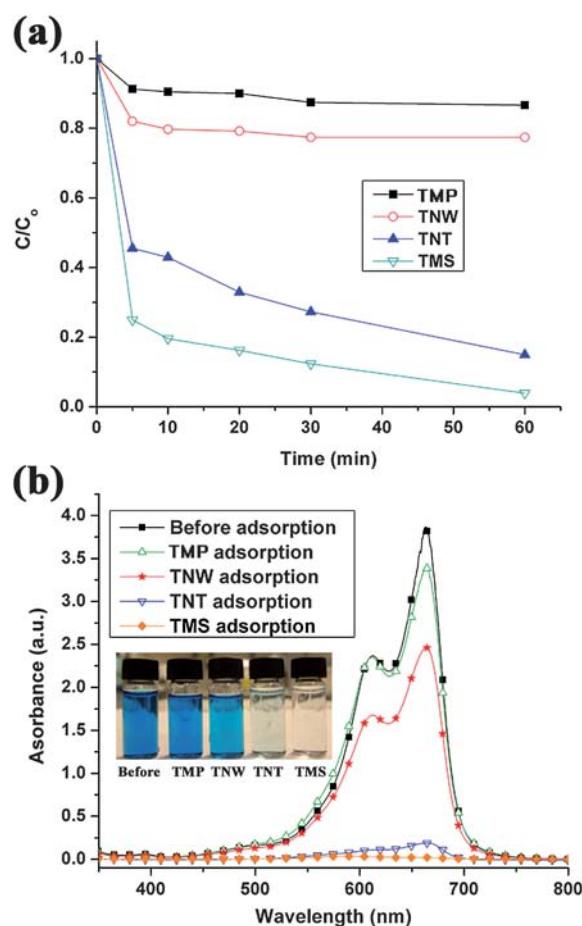


Fig. 9 (a) Adsorption MB (20 ppm, 50 mL) by TMP, TNW, TNT, and TMS. C_0 (ppm) is the initial concentration of the MB solution and C (ppm) is the concentration of that at different intervals during the adsorption. (b) Comparison of the absorption spectra of the MB solution (20 ppm, 50 mL) before and after 12 h adsorption and in the presence of TMP, TNW, TNT and TMS. The amount of adsorbent is 10 mg, and photographs showing the solution color are, from left to right, before adsorption, TMP, TNW, TNT and TMS.

titanate spheres.^{3,15} The TMS also shows excellent adsorption performance of Pb^{II} ions (Fig. 10). Similar to the adsorption rate of MB, the adsorption of Pb^{II} onto TMS was the fastest. The TMS was able to remove Pb^{II} from the solution almost completely in less than 10 min, as evidenced by the concentration decrease from 120.5 mg L^{-1} (C_0) to less than 0.5 mg L^{-1} at room temperature (Fig. 10a). In addition, the as-prepared TMS possesses excellent adsorption capacities of Pb^{II} toxic ion. The plateau saturation capacities based on the isotherm curves in Fig. 10b are 0.56 mmol g^{-1} for TMP, 2.41 mmol g^{-1} for TMS, 2.60 mmol g^{-1} for TNT and 2.62 mmol g^{-1} for TNW titanate materials (Table 1). The capacity of TMS is greater than TMP and comparable with the 1D nanostructure titanate (TNT, TNW).

Comparing the performance among the four types of titanate in MB and Pb^{II} adsorption, we believe that the adsorption mechanisms are different, which have resulted in the difference in the observed removal capacity. MB is cationic dye; the electrostatic force between the adsorbent and the MB ions plays an

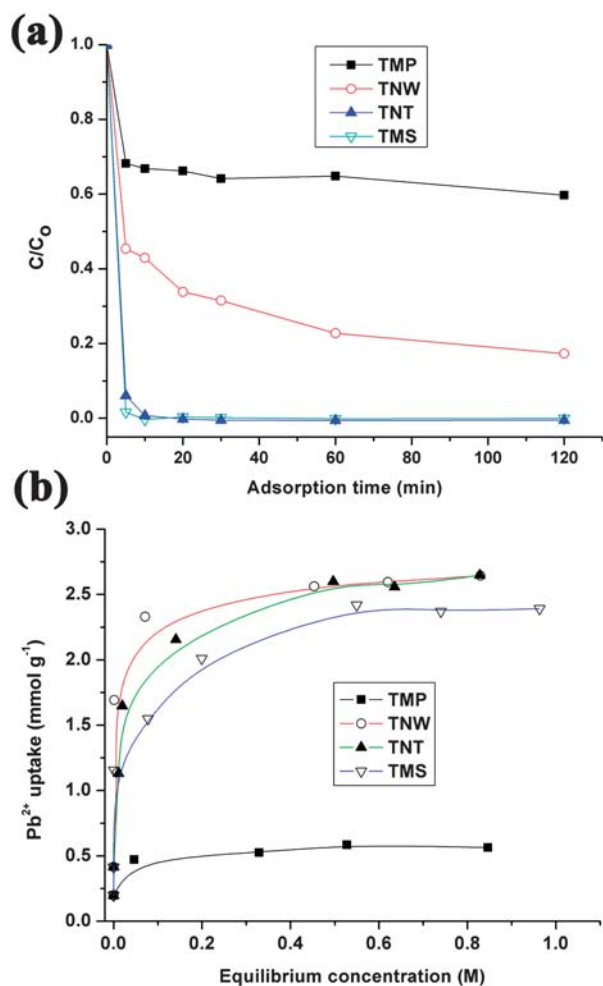


Fig. 10 Comparison of (a) adsorption rate and (b) adsorption isotherms of Pb^{II} ions by TMP, TNW, TNT and TMS. C_0 (120.5 mg L^{-1}) is the initial Pb^{II} concentration, and C the concentration at different intervals during the test.

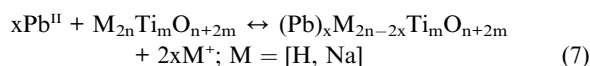
Table 1 BET surface area and removal capacity of different adsorbent samples

Absorbent samples	BET surface area [$\text{m}^2 \text{ g}^{-1}$]	Experimental capacity for MB [mg g^{-1}]	Experimental capacity for Pb^{II} [mmol g^{-1}]
TMP	1.07	80.8 ± 7.4	0.56 ± 0.03
TNW	13.82	94.6 ± 4.5	2.62 ± 0.06
TNT	157.64	232.2 ± 11.0	2.60 ± 0.05
TMS	277.52	236.2 ± 10.3	2.41 ± 0.06

important role in its adsorption capacity. To verify this, we performed Zeta potential measurement of the TNT in different pH values (Fig. S10a, ESI \dagger) and their corresponding adsorptions of an initial concentration of 20 ppm MB solution are shown in Fig. S10b. The highest MB dye removal occurs at pH 9.5~10 when the titanate surface is most negatively charged. Varying the solution pH affects the adsorption; there was very little MB adsorption when pH = 1 (Fig. S10b, ESI \dagger). Therefore, all the other adsorption performance of titanate materials was performed at pH 9.5~10. The data in Table 1 suggest that the

adsorption capacity increases with increasing surface area. It was suggested that MB molecules might be trapped into the interlayer space of the titanate by exchanging with cation ions.³ However since MB is a larger molecule, we do not expect such an exchange would only occur at sites near the particle surfaces. In other words, the MB adsorption capacity is highly sensitive to the surface area. Therefore it is not surprising that the TMS sample with the hierarchical porous structure as described earlier gives rise to the highest MB adsorption rate and capacity (Fig. 9 and Table 1).

The Pb^{II} adsorption by the titanates is through ion-exchange which was evidenced by XRD and Raman measurements,^{6a, 6d, 27} i.e., the Pb^{II} cations replace the protons or Na^+ via the following reaction:



The cation exchange capacity ($\text{CEC} = \text{mol}_{\text{Na,H}}/\text{M}_{\text{w}}(\text{titanate})$) of titanate material is mainly depended on the exchange-able sites in the adsorbent. It was found that the exchange capacities of TMS, TNW and TMP are high and comparable, but the one for the TMP is much lower (Table 1). The poor sorption performance of TMP is due to its large particle size which effectively hinders the cation diffusion during the exchange process. As shown in Fig. S7 (ESI \dagger), the particle size of the TMP is around 1~2 μm . In comparison, the TMS sample also has large particle size, but its hierarchical porous structure facilitates the exchange reaction extending to large number of exchangeable sites.

In addition to the morphological reason, the crystal structure may also play an role in the adsorption performance.^{6a,27a} The TMP ($\text{Na}_2\text{Ti}_3\text{O}_7$) synthesized by high temperature solid state reaction has a different crystal structure with the one by low temperature solution process. The former has a theoretical cation exchange capacity 6.62 mmol g^{-1} , which is lower than the one for TMS ($\text{Na}_{2-x}\text{H}_x\text{Ti}_2\text{O}_5$, 9.05 mmol g^{-1}). Therefore, the surface area and the crystal structure are the main factors that give rise to the excellent adsorption rate and capacity of the TMS particles. Compared with the titanate TMP, TNW and TNT, the TMS has the fastest adsorption rate which is clearly related to its high surface area. Therefore, it is the most efficient adsorbent in terms of sorption kinetics for removal of the MB organic dye and Pb^{II} heavy metal ions from contaminated water. In addition, as the size of the TMS sample is of the order of micrometres, the particles will not easily agglomerate. The recovery of the used particles will be much easier than nanoparticles. From a practical application point of view, our synthesized TMS also enjoys a clear advantage in terms of production and operation cost.

Conclusion

We have successfully developed a fast and facile synthesis of 3D TMS with a high specific surface area by a low-cost and simple ESDS method in alkaline solution at an ambient setup. The formation process is led by the concurrent anodic reaction oxidation and the electrical breakdown of the formed oxide layer into the electrolyte in precipitate form. The spallation is driven by a continuous spark discharge that simultaneously heat up the solution. The TiO_2 precipitates then react immediately with the

heated NaOH solution to form the TMS particles. The as-prepared TMS powders show excellent ion-exchange ability and high adsorption rate with toxic Pb^{II} ion and the MB dye due to its specific hierarchical structure and crystal structure. The current work creates a novel route to synthesis titanate superstructures with unique morphologies and complex hierarchies at the micro- and nanoscale in short processing time. We expect a wide range of applications for this type of materials in photocatalysis and energy storage when excellent functionality and large surface area are essential.

Acknowledgements

The authors thank the National Research Foundation of Singapore Government (grant MEWR651/06/160) for the financial support of the work. Technical assistance from Prof. T.-T. Lim, Mr K.-H. Goh, Ms Jun Guo, and Mr Lizhi Zhang are gratefully acknowledged. The authors would like to thank the anonymous reviewers for their constructive comments and suggestions which have helped us to improve the discussion of the formation mechanism of TMS.

Notes and references

- 1 J. S. Hu, L. S. Zhong, W. G. Song and L. J. Wan, *Adv. Mater.*, 2008, **20**, 2977.
- 2 (a) Y. Li, T. Sasaki, Y. Shimizu and N. Koshizaki, *J. Am. Chem. Soc.*, 2008, **130**, 14755; (b) C. F. Xue, J. X. Wang, B. Tu and D. Y. Zhao, *Chem. Mater.*, 2010, **22**, 494; (c) Y. Q. Dai, X. F. Lu, M. McKiernan, E. P. Lee, Y. M. Sun and Y. N. Xia, *J. Mater. Chem.*, 2010, **20**, 3157; (d) S. H. Sun, G. W. Meng, G. X. Zhang, J. P. Masse and L. Zhang, *Chem.–Eur. J.*, 2007, **13**, 9087; (e) D. Gu, H. Bongard, Y. H. Deng, D. Feng, Z. X. Wu, Y. Fang, J. J. Mao, B. Tu, F. Schuth and D. Y. Zhao, *Adv. Mater.*, 2010, **22**, 833.
- 3 Y. Takezawa and H. Imai, *Small*, 2006, **2**, 390.
- 4 H. J. Liu, X. M. Wang, W. J. Cui, Y. Q. Dou, D. Y. Zhao and Y. Y. Xia, *J. Mater. Chem.*, 2010, **20**, 4223.
- 5 (a) T. Kasuga, M. Hiramatsu, A. Hoson, T. Sekino and K. Niihara, *Langmuir*, 1998, **14**, 3160; (b) T. Kasuga, M. Hiramatsu, A. Hoson, T. Sekino and K. Niihara, *Adv. Mater.*, 1999, **11**, 1307.
- 6 (a) D. J. Yang, Z. F. Zheng, H. Y. Zhu, H. W. Liu and X. P. Gao, *Adv. Mater.*, 2008, **20**, 2777; (b) A. Riss, M. J. Elser, J. Bernardi and O. Diwald, *J. Am. Chem. Soc.*, 2009, **131**, 6198; (c) H. Y. Niu, J. M. Wang, Y. L. Shi, Y. Q. Cai and F. S. Wei, *Microporous Mesoporous Mater.*, 2009, **122**, 28; (d) D. V. Bavykin, J. M. Friedrich and F. C. Walsh, *Adv. Mater.*, 2006, **18**, 2807; (e) Y. K. Lai, Y. C. Chen, Y. X. Tang, D. G. Gong, Z. Chen and C. J. Lin, *Electrochem. Commun.*, 2009, **11**, 2268.
- 7 (a) X. M. Sun and Y. D. Li, *Chem.–Eur. J.*, 2003, **9**, 2229; (b) Q. Chen, W. Z. Zhou, G. H. Du and L. M. Peng, *Adv. Mater.*, 2002, **14**, 1208; (c) R. Z. Ma, Y. Bando and T. Sasaki, *Chem. Phys. Lett.*, 2003, **380**, 577; (d) C. C. Tsai and H. S. Teng, *Chem. Mater.*, 2004, **16**, 4352; (e) Y. Suzuki and S. Yoshikawa, *J. Mater. Res.*, 2004, **19**, 982.
- 8 (a) H. Y. Zhu, Y. Lan, X. P. Gao, S. P. Ringer, Z. F. Zheng, D. Y. Song and J. C. Zhao, *J. Am. Chem. Soc.*, 2005, **127**, 6730; (b) T. Zhang, Q. Chen and L. M. Peng, *Adv. Funct. Mater.*, 2008, **18**, 3018.
- 9 Z. Liu, T. Yamazaki, Y. Shen, D. Meng, T. Kikuta and N. Nakatani, *J. Phys. Chem. C*, 2008, **112**, 4545.
- 10 R. A. Doong and I. L. Kao, *Recent Pat. Nanotechnol.*, 2008, **2**, 84.
- 11 J. Q. Huang, Z. Huang, W. Guo, M. L. Wang, Y. G. Cao and M. C. Hong, *Cryst. Growth Des.*, 2008, **8**, 2444.
- 12 (a) T. Sasaki and M. Watanabe, *J. Am. Chem. Soc.*, 1998, **120**, 4682; (b) T. Sasaki, Y. Ebina, Y. Kitami, M. Watanabe and T. Oikawa, *J. Phys. Chem. B*, 2001, **105**, 6116; (c) N. Miyamoto, K. Kuroda and M. Ogawa, *J. Mater. Chem.*, 2004, **14**, 165; (d) T. Gao, H. Fjellvag and P. Norby, *J. Phys. Chem. B*, 2008, **112**, 9400; (e) J. H. Choy, H. C. Lee, H. Jung and S. J. Hwang, *J. Mater. Chem.*, 2001, **11**, 2232.
- 13 Y. B. Mao, M. Kanungo, T. Hemraj-Benny and S. S. Wong, *J. Phys. Chem. B*, 2006, **110**, 702.
- 14 J. Jitputti, T. Rattanavoravipa, S. Chuangchote, S. Pavasupree, Y. Suzuki and S. Yoshikawa, *Catal. Commun.*, 2009, **10**, 378.
- 15 C. W. Peng, T. Y. Ke, L. Brohan, M. Richard-Plouet, J. C. Huang, E. Puzenat, H. T. Chiu and C. Y. Lee, *Chem. Mater.*, 2008, **20**, 2426.
- 16 C. Wu, L. Lei, X. Zhu, J. Yang and Y. Xie, *Small*, 2007, **3**, 1518.
- 17 (a) G. K. Mor, O. K. Varghese, M. Paulose, K. Shankar and C. A. Grimes, *Sol. Energy Mater. Sol. Cells*, 2006, **90**, 2011; (b) A. Ghicov and P. Schmuki, *Chem. Commun.*, 2009, 2791; (c) R. Hahn, T. Stergiououlus, J. M. Macak, D. Tsoukleris, A. G. Kontos, S. P. Albu, D. Kim, A. Ghicov, J. Kunze, P. Falaras and P. Schmuki, *Phys. Status Solidi RRL*, 2007, **1**, 135; (d) K. Shankar, J. I. Basham, N. K. Allam, O. K. Varghese, G. K. Mor, X. J. Feng, M. Paulose, J. A. Seabold, K. S. Choi and C. A. Grimes, *J. Phys. Chem. C*, 2009, **113**, 6327.
- 18 (a) A. L. Yerokhin, X. Nie, A. Leyland, A. Matthews and S. J. Dowey, *Surf. Coat. Technol.*, 1999, **122**, 73–93; (b) L. H. Li, Y. M. Kong, H. W. Kim, Y. W. Kim, H. E. Kim, S. J. Heo and J. Y. Koak, *Biomaterials*, 2004, **25**, 2867; (c) Y. Han, S. H. Hong and K. W. Xu, *Surf. Coat. Technol.*, 2003, **168**, 249.
- 19 (a) Y. X. Tang, Y. K. Lai, D. G. Gong, K.-H. Goh, T.-T. Lim, Z. L. Dong and Z. Chen, *Chem.–Eur. J.*, 2010, **16**, 7704; (b) Y. K. Lai, C. J. Lin, J. Y. Huang, H. F. Zhuang, L. Sun and T. Nguyen, *Langmuir*, 2008, **24**, 3867; (c) Y. K. Lai, X. F. Gao, H. F. Zhuang, J. Y. Huang, C. J. Lin and L. Jiang, *Adv. Mater.*, 2009, **21**, 3799.
- 20 (a) G. Liu, L. Z. Wang, C. H. Sun, X. X. Yan, X. W. Wang, Z. G. Chen, S. C. Smith, H. M. Cheng and G. Q. Lu, *Chem. Mater.*, 2009, **21**, 1266; (b) T. W. Kim, S. G. Hur, S. J. Hwang, H. Park, W. Choi and J. H. Choy, *Adv. Funct. Mater.*, 2007, **17**, 307.
- 21 T. Gao, H. Fjellvag and P. Norby, *Inorg. Chem.*, 2009, **48**, 1423.
- 22 C. C. Tsai and H. S. Teng, *Chem. Mater.*, 2006, **18**, 367.
- 23 (a) D. A. Vermilyea, *Acta Metall.*, 1953, **1**, 282; (b) L. Young, *Trans. Faraday Soc.*, 1954, **50**, 153.
- 24 H. M. Kim, F. Miyaji, T. Kokubo and T. Nakamura, *J. Mater. Sci.: Mater. Med.*, 1997, **8**, 341.
- 25 C. K. Lee, K. S. Lin, C. F. Wu, M. D. Lyu and C. C. Lo, *J. Hazard. Mater.*, 2008, **150**, 494.
- 26 (a) M. R. Huang, Q. Y. Peng and X. G. Li, *Chem.–Eur. J.*, 2006, **12**, 4341; (b) X. J. Ju, S. B. Zhang, M. Y. Zhou, R. Xie, L. Yang and L. Y. Chu, *J. Hazard. Mater.*, 2009, **167**, 114.
- 27 (a) D. J. Yang, Z. F. Zheng, H. W. Liu, H. Y. Zhu, X. B. Ke, Y. Xu, D. Wu and Y. Sun, *J. Phys. Chem. C*, 2008, **112**, 16275; (b) H. Kochkar, A. Turki, L. Bergaoui, G. Berhault and A. Ghorbel, *J. Colloid Interface Sci.*, 2009, **331**, 27.